CHEMISTRY OF MATERIALS

pubs.acs.org/cm

Article

Equilibrium Particle Shape and Surface Chemistry of Disordered Li-Excess, Mn-Rich Li-ion Cathodes through First-Principles Modeling

Jordan Burns,* Bin Ouyang, Jianli Cheng, Matthew K. Horton, Martin Siron, Oxana Andriuc, Ruoxi Yang, Gerbrand Ceder, and Kristin A. Persson*

Cite This: https://doi.org/10.1021/acs.chemmater.2c00804

Read Online

ACCESS | Metrics & More | Article Recommendations

ABSTRACT: A novel methodology for calculating the surface energy of a disordered material was developed and is described here. The method was used to calculate the range of surface energies for {100}, {110}, {111}, and {112} type facets of the disordered rock salt (DRX) cathode material Li_2MnO_2F, as a function of surface cation and anion decoration. Boltzmann averaging was used to determine average surface energies for each facet which were then used to calculate the equilibrium particle shape. It was found that Li_2MnO_2F displays predominantly {100} type lithium/fluorine-rich facets favoring a cubic particle shape. The density of states along with electronic structure-based bonding analyses are calculated to rationalize differences observed in surface energy. Importantly, it is found that surface lithium and fluorine lower the surface energy of the majority facets, suggesting that surfaces of Li_2MnO_2F are likely enriched in lithium and fluorine and display less oxygen and manganese, which has implications for capacity and rate retention.

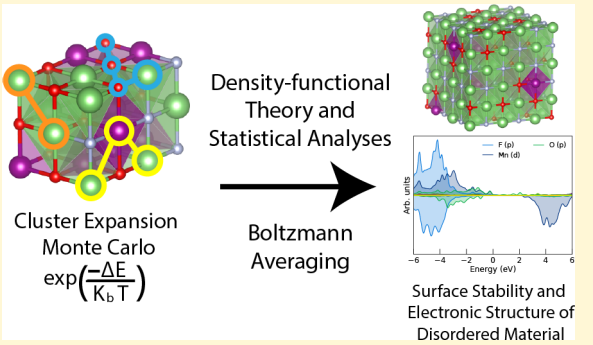

INTRODUCTION

The pressing need to incorporate renewable energy sources into the power grid to combat climate change combined with the rapid growth of electrified transportation is driving the demand for increased production and innovation of rechargeable batteries.[1,2] Conventional, rechargeable lithium-ion batteries based on the layered cathode family rely on cobalt and nickel, where the sourcing of cobalt presents serious resource as well as geopolitical concerns,[3,4] and even global nickel production is unlikely to sustain the projected growth of the battery industry.[5] Disordered lithium-excess rocksalt (DRX) materials are a chemically diverse set of materials that offer the potential for cobalt-free, high-energy-density, and affordable cathode materials.[6−8] However, most lithium excess cathodes suffer from surface oxygen loss and the resulting impedance buildup and capacity fade.[9−14] Interestingly, DRX materials can be highly fluorinated, substituting oxygen for fluorine throughout the bulk of the material.[15−18] It is conjectured that such fluorination — if prevalent at particle surfaces — has the potential to mitigate surface reactivity, while also lowering the overall bulk metal charge states to increase the metal redox activity at high charge, as compared to oxygen.[19−23]

Previous work has attempted to elucidate the mechanisms by which fluorination guards against oxygen loss through investigating the surface chemistry and particle morphology of DRX materials. Experimental work by Kwon et al. found that, through cycling, metal densification occurs on the surface of the DRX materials $Li_{1.2}Ni_{0.333}Ti_{0.333}Mo_{0.133}O_2$ (LNTMO) and $Li_{1.2}Mn_{0.6}Nb_{0.2}O_2$ (LMNO) and that, additionally, a spinel structure forms on the surface of LMNO.[24] Li et al., studying the DRX compound $Li_{1.2}Ti_{0.4}Mn_{0.4}O_{2.0}$ (LTMO), and its fluorinated version, $Li_{1.2}Ti_{0.2}Mn_{0.6}O_{1.8}F_{0.2}$ (LTMOF), found that both materials in their pristine states display crystallinity throughout their bulk and surface regions. However, after 50 cycles, LTMO develops amorphous regions and voids that initiate at the surface, in contrast to LTMOF, which maintains crystallinity at the surface after 50 cycles.[25] Chen et al. found that, upon cycling the DRX materials $Li_{1.3}Ti_{0.3}Mn_{0.4}O_{1.7}F_{0.3}$ and $Li_{1.2}Ti_{0.2}Mn_{0.6}O_{1.8}F_{0.2}$, fluorine enrichment occurred on the surface, along with the formation of Li−F-like domains.[26] Previous computational work studying the ordered, unfluorinated compound Li_2MnO_3 found that the predominant surface facets of the equilibrium particle shape are (001) and (010).[27] Karim et al. showed for the first time that previous

Received: March 15, 2022
Revised: July 25, 2022

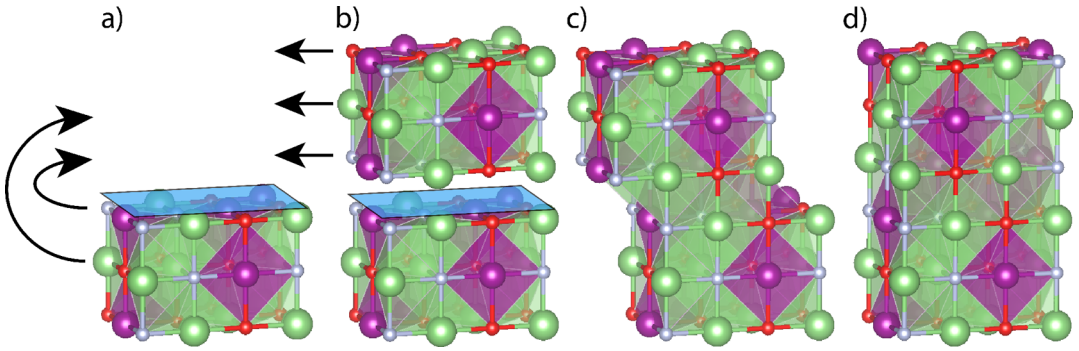

Figure 1. Stepwise procedure for creating bulk structures for surface calculations of a disordered material is shown for a {100} type surface. (a) Initial structures are obtained from Monte Carlo simulations based on a cluster expansion. The arrow provides a guide to the eye for mirroring the structure across the indicated plane. (b) The initial structure is mirrored across the plane and the arrows indicate the direction of translation of the structure to preserve FCC cation−anion ordering. (c) The resulting structure after applying the mirror and translational operations. (d) Periodic boundary conditions are applied to show the atoms inside of the boundary of the final bulk structure with symmetric surfaces.

disagreement between the calculated equilibrium particle shape for spinel $LiMn_2O_4$ and experimental observations was due to cation site surface reconstruction, which stabilizes the {111} facet.[28] In both these cases, it was found that surface manganese is energetically unfavorable and that it prefers to exchange sites with subsurface lithium,[27,28] effectively creating a surface inverse spinel cation decoration. Other investigations of cathode materials have found a large energy penalty for under-coordinated manganese on the surface as well.[9,29]

However, there has been limited exploration of disordered materials from a surface chemistry and particle morphology perspective. The Wulff construction was modified by Ringe et al. to study the size dependence of the equilibrium particle shapes of alloy nanoparticles,[30] accounting for disorder through the degree to which species are favored to segregate. To the authors' knowledge, disordered oxides have not been subjected to any computational determination of their preferred surface chemistry and resulting equilibrium particle shapes, in particular no computational surface investigations of the DRX compound Li_2MnO_2F have been published.

Here, we present a novel methodology to model the surfaces of disordered oxides and apply the model to the lithium excess, manganese-rich DRX compound Li_2MnO_2F. Results from a previous cluster expansion model,[31,32] trained using ab initio calculations as described in Ouyang et al.,[20] are used as a basis for Monte Carlo simulations to create and equilibrate the disordered bulk structures.[33−35] Symmetric surfaces are created artificially from these structures by mirroring the structure, and specifically the surface, across the desired surface plane and then rotating and/or translating the mirrored portion as necessary to preserve its basic FCC anion and cation arrangement. This approach enables a robust ab initio calculation of surface energies and we apply it to various surface chemistries of {100}, {110}, {111}, and {112} type facets for the overall stoichiometry Li_2MnO_2F, a representative lithium-excess, manganese-rich, fluorinated cathode composition. Capturing the spread in energies as a function of surface cation and anion decoration, we use Boltzmann averaging to determine the most likely energy of each facet, which are then used to construct the equilibrium particle shape.

METHODS

Density Functional Theory Calculations. All first-principles calculations were performed using the Vienna Ab-Initio Simulation Package (VASP),[36−39] using the projector augmented-wave (PAW) potentials[40] with the Perdew−Burke−Ernzerhof (PBE) generalized-gradient approximation (GGA) functional.[41] Structure optimization calculations were used to fully relax atomic positions and lattice parameters in bulk structures. Slab optimizations were used to fully relax the atomic positions of the three outermost surface layers of the slabs using at least 15 Å of vacuum. Both bulk and slab total energies were further improved using static calculations. Non-self-consistent calculations were performed on the output from self-consistent static calculations keeping the charge density the same but increasing the *k*-point mesh. All INCAR parameters used were benchmarked by the Materials Project and are documented in MPRelaxSet, MPStaticSet, and MPNonSCFSet in Python Materials Genomics (pymatgen).[42]

Generating Disordered Bulk and Surface Structures. All bulk structures were generated using Monte Carlo simulations based on a previously obtained cluster expansion.[20] Structures were equilibrated with at least 100 000 Monte Carlo steps and then structures were sampled during a production run of at least 100 000 Monte Carlo steps at a temperature of 2573 °C. In order to generate symmetric surfaces for the disordered material, a novel method was employed as illustrated in Figure 1. One unit cell of the bulk structure was first mirrored across the plane parallel to the facet of study. The mirrored portion was then translated and/or rotated in the same plane to maintain a proper FCC anion and cation arrangement. We note that the resulting unit-cell structure has doubled in size, compared to the original one, but retains both stoichiometry and crystal structure. Most importantly, the resulting doubled unit cell exhibits symmetric terminations in the desirable direction (to a translation and rotation). Bulk structure relaxations as described in the DFT section were then performed and the resulting relaxed structures were used to create supercells of dimensions (1, 1, 2). Slab calculations were then performed as described in the DFT section.

Surface Energy Calculation. The total energy output from the bulk and slab calculations, along with the dimensions of the surface of the slab, were used to calculate the surface energy according to the following equation:

$$\gamma = \frac{E_{\text{slab}} - N \cdot E_{\text{bulk}}}{2A} \tag{1}$$

where γ is the surface energy, E_{slab} the total energy output of the slab calculation, N the number of bulk layers in the supercell (two for all calculations reported here), E_{bulk} the total energy of the bulk calculation of the parent bulk structure of each specific surface, and A the surface area of the slab. The entire workflow is illustrated in Figure 2.

Equilibrium Particle Shape Calculation. Boltzmann weighting is performed according to the following equation:

$$\gamma_{\text{Boltzmann}} = \frac{\sum_i w_i \gamma_i}{\sum_i w_i} \tag{2}$$

https://doi.org/10.1021/acs.chemmater.2c00804
Chem. Mater. XXXX, XXX, XXX−XXX

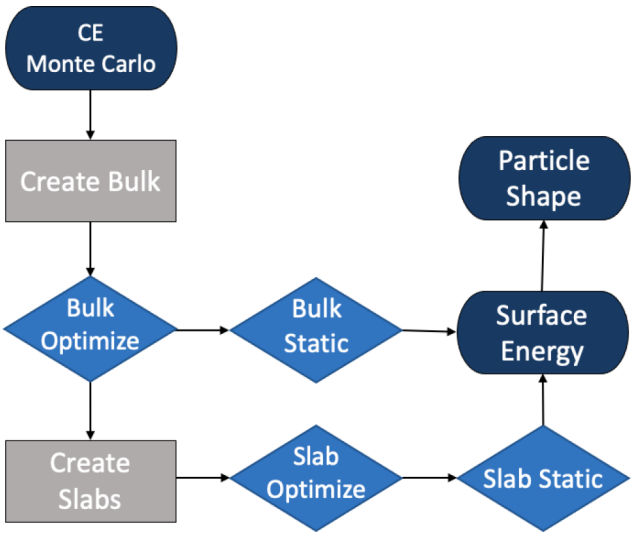

Figure 2. Illustration of the workflow for calculating the surface energy of a disordered oxide. Dark blue ovals indicate simulations or application of algorithms in python, gray boxes are structure manipulations with pymatgen, and blue diamonds are VASP calculations.

where $\gamma_{\text{Boltzmann}}$ is the Boltzmann-weighted surface energy for a given facet, γ_i is the surface energy of surface i, and w_i is defined as

$$w_i = \Omega_i \exp\left(\frac{E_i - E_0}{k_B T}\right) \tag{3}$$

where Ω_i is the multiplicity of surface i, E_i the per atom energy difference between the slab and its corresponding bulk energy for surface i, E_0 the lowest per atom energy difference calculated for the given facet, k_B the Boltzmann constant, and T the temperature (0 K and 298 K). The multiplicities for each possible surface were found by taking statistics from at least 1 000 000 surfaces generated from Monte Carlo structures for each facet. Laplace smoothing (also called additive smoothing) with an α value of 1 was applied to the multiplicities. Currently, it is intractable to calculate the millions of possible surface energies needed to fully satisfy this equation. Hence, the calculated surface energies are considered a sample that approximate the larger population of possible surface energies. These equations were used to calculate a Boltzmann-weighted average surface energy for each facet and the Boltzmann-weighted surface energy for each facet is used to calculate the equilibrium particle shape, as implemented in pymatgen.[42,43]

Bonding Analysis. In order to analyze the bonding and antibonding character at the surface of the disordered structures, a Crystal Orbital Hamiltonian Population analysis was performed using the Local-Orbital Basis Suite Toward Electronic-Structure Reconstruction (LOBSTER) package.[44−47] The output of the density of states calculations were utilized, obtaining results with <1% charge spilling. LOBSTER input parameters were generated using pymatgen and all interactions within 6 Å were calculated.

RESULTS AND DISCUSSION

Surface energies were obtained from bulk and slab calculations of {100}, {110}, {111}, and {112} type facets of various disordered bulk configurations and surface terminations of Li_2MnO_2F, resulting in 195 distinct surface energy data points. Figure 3 shows the spread of calculated surface energies for different ionic surface as well as bulk configurations, for each crystal facet. We note that {100} type surfaces exhibit the lowest energies, and a fairly narrow energy distribution across different ionic orderings, followed by {110} type surfaces. The

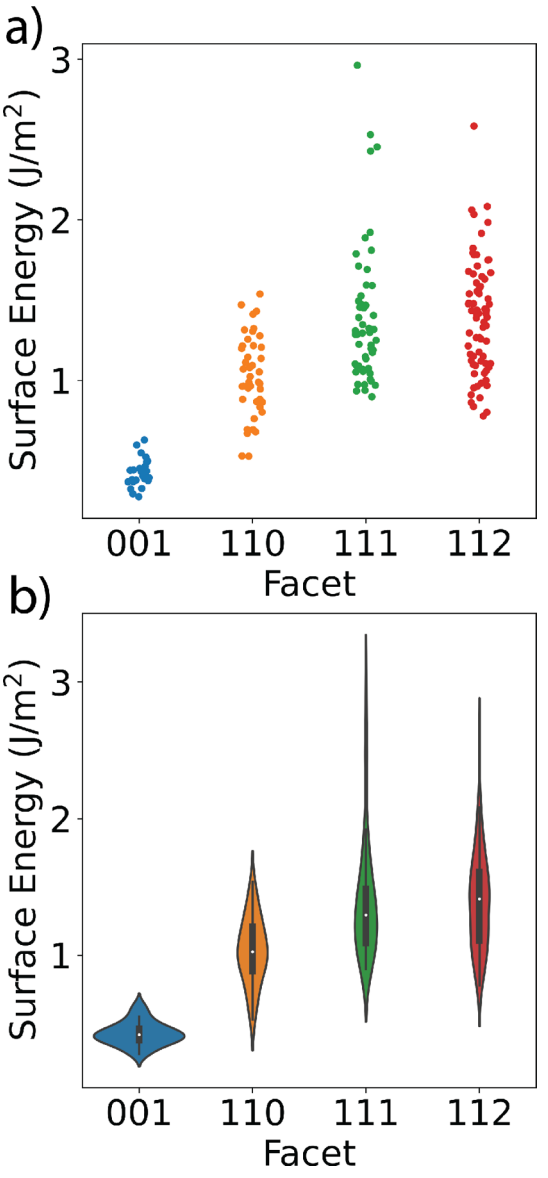

Figure 3. Calculated surface energies as a function of facet, for a broad range of surface as well as bulk ionic configurations corresponding to the possible variations in disordered rocksalt Li_2MnO_2F. (a) All data points are plotted with a small variation along the x-axis to improve their visibility. (b) A violin plot is shown, which emphasizes the distribution of points along the surface energy axis.

Table 1. Calculated Boltzmann Weighted Surface Energies Are Presented for Each Facet at 0 K and 298 K

	Boltzmann-Weighted Surface Energy (J/m^2)	
facet	0 K	298 K
{100}	0.27	0.43
{110}	0.53	0.78
{111}	0.90	1.00
{112}	0.78	0.85

distribution of surface energies originating from {110}, {111}, and {112} type facets skew significantly higher than {100}. Correspondingly, the standard deviation in surface energy of {100} is 0.09 J/m^2, whereas it is 0.24, 0.43, and 0.35 J/m^2 for {110}, {111}, and {112}, respectively.

https://doi.org/10.1021/acs.chemmater.2c00804
Chem. Mater. XXXX, XXX, XXX−XXX

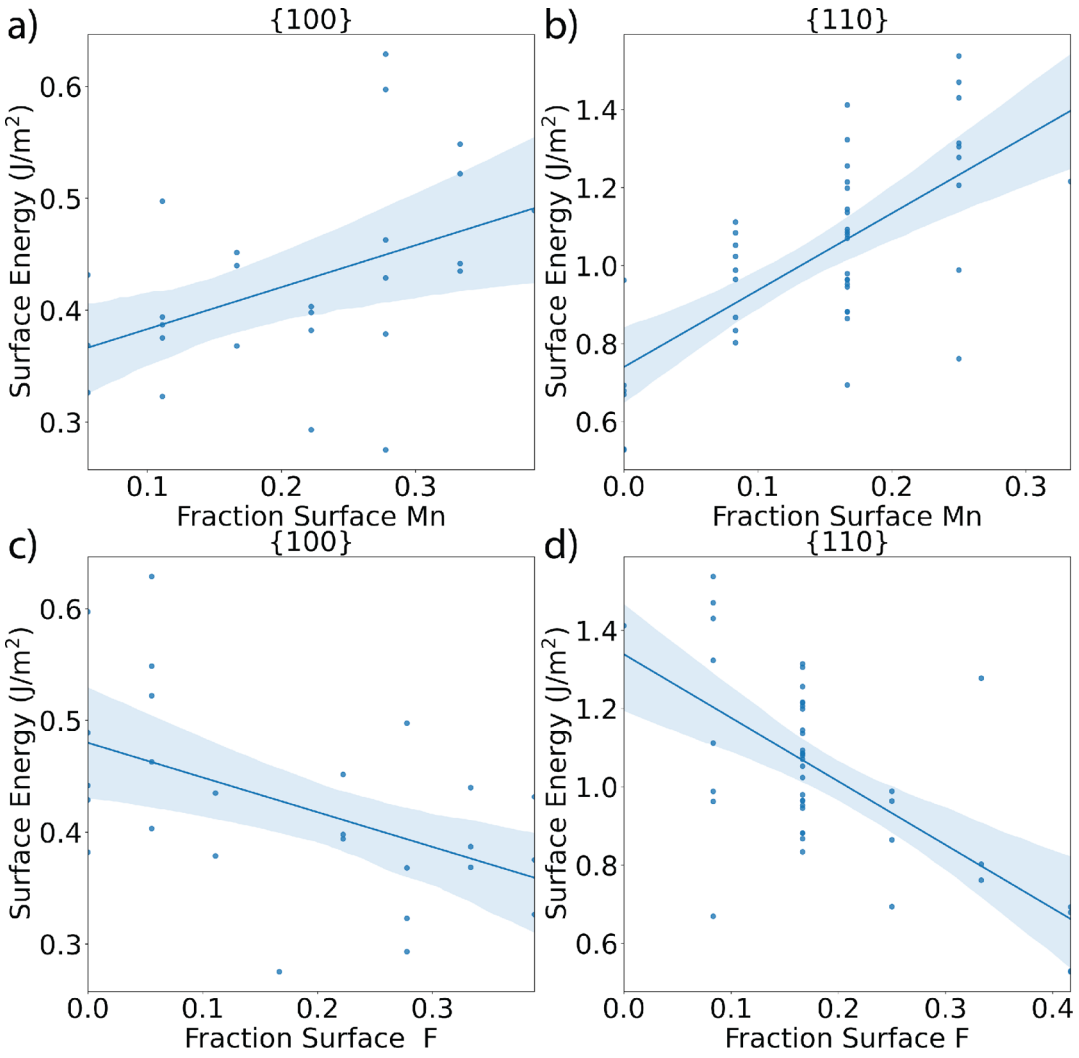

Figure 4. Linear regression was performed to estimate the relationship between surface energy and surface chemistry for {100} and {110}. A line of best fit is shown along with a 95% confidence interval for the line of best fit computed by sampling the data 1000 times. Panel (a) shows the surface energy versus the surface manganese for {100}, panel (b) shows the surface energy versus the surface manganese for {110}, panel (c) shows the surface energy versus the surface fluorine for {100}, and panel (d) shows the surface energy versus the surface fluorine for {110}.

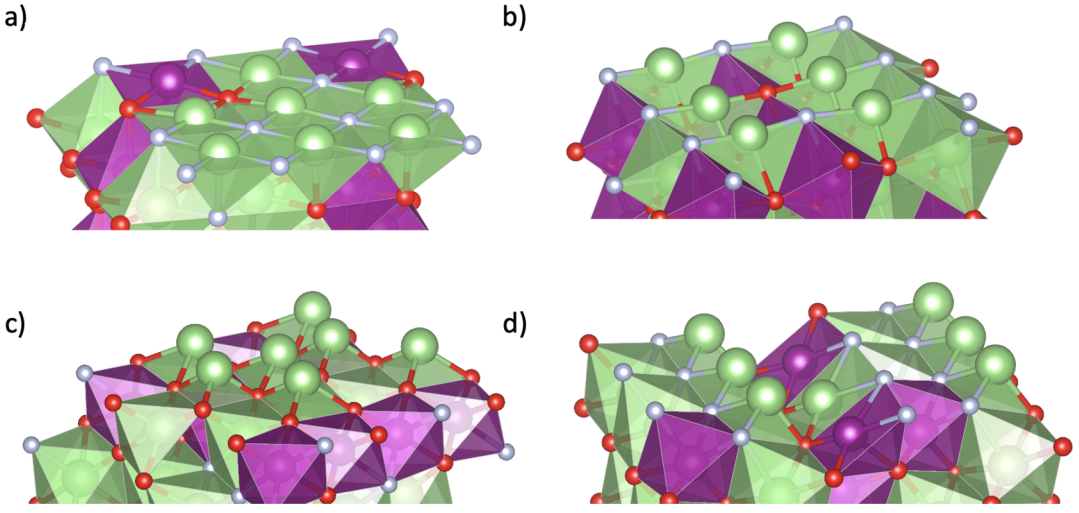

Figure 5. Lowest energy surface calculated for each facet is shown: (a) {100}, (b) {110}, (c) {111}, and (d) {112}. Green atoms are Li, purple atoms are Mn, red atoms are O, and gray atoms are F.

https://doi.org/10.1021/acs.chemmater.2c00804
Chem. Mater. XXXX, XXX, XXX−XXX

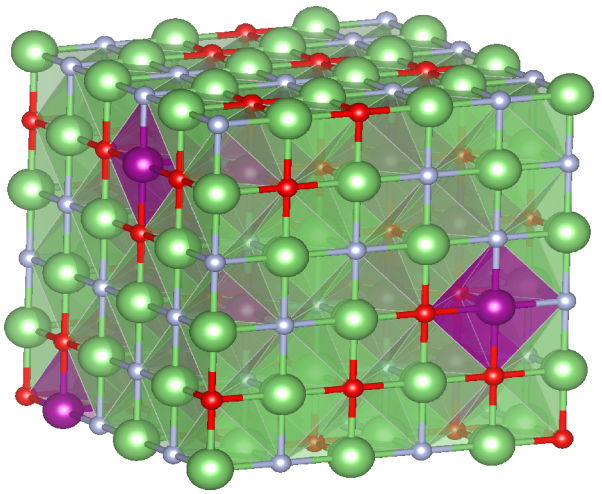

Figure 6. Equilibirum particle shape for Li_2MnO_2F is shown. {100} type surfaces dominate to create a cubic shape.

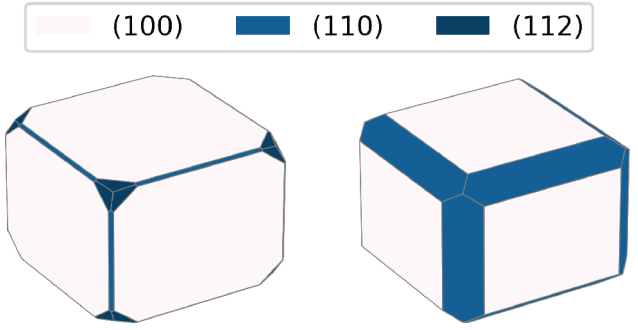

Figure 7. Equilibrium particle shapes that deviated most strongly from a cube shape from the 10 000 resamplings of the surface energy data are shown.

In order to obtain a single energy value for each facet to calculate the equilibrium particle shape, Boltzmann weighting was used to represent the surface energy by ensemble average at the temperatures of 0 and 298 K. As elaborated on in the Methods section, we treat the calculated surface energies as a sample of the larger population of possible surface energies. The Boltzmann weighted energies are presented in Table 1. From this set, the equilibrium particle shape was obtained using the pymatgen's Wulff Shape analysis class.[48] In agreement with the distributions of energies in Figure 3, the dominant facets are of type {100}. The Boltzmann weighted surface energy for the {100} type facet is significantly lower than the others, which results in a {100}-dominated cube equilibrium particle shape. Experimental work in the literature report DRX materials exposing {100} and {110} type facets, in good agreement with our computational results. Kwon et al. show high-resolution scanning transmission electron microscope images observing a {110} type facet of the DRX material $Li_{1.2}Ni_{0.333}Ti_{0.333}Mo_{0.133}O_2$.[24] In the DRX material $Li_{1.3}Ti_{0.3}Mn_{0.4}O_{1.7}F_{0.3}$ Chen et al. observed directional cracking along the ⟨100⟩ family of directions exposing {100} type planes.[49]

To elucidate the effect of surface chemistry on surface energy we employ a bootstrapping statistical method, which uses results found on a collection of smaller random samples to infer properties of the entire population, using replacement during the sampling process. For clarity, when referring to the

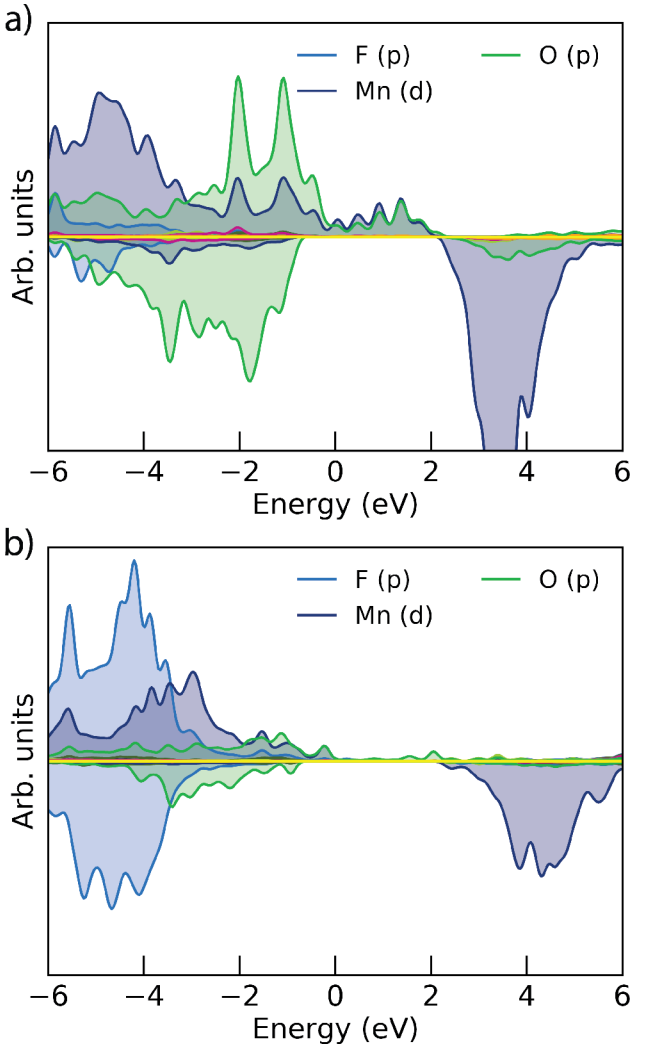

Figure 8. Partial density of states are plotted for (a) the highest energy {100} surface and (b) the lowest energy {100} surface. Only the density of states from the outermost surface layer is plotted. States below the *x*-axis are spin down and states above the *x*-axis are spin up.

surface, only the outermost layer of atoms is considered. A linear regression model as implemented in Seaborn[50] was used to calculate the line of best fit and a 95% confidence interval for the line by sampling the data 1000 times, as shown in Figure 4. Inside of the 95% confidence interval for both {100} and {110} facets, increasing the surface manganese increased the predicted surface energy, while increasing the surface fluorine content had the opposite effect. We also observe that the surface manganese has a greater effect of improving stability of {100} type surfaces, compared to {110} type surfaces. We find that some of the lower energy {100} surfaces contain a small amount of manganese while the lowest energy {110} surface does not contain any. Previous work[28] shows that manganese is particularly sensitive to undercoordination and, in that context, we note that the {110} surfaces exhibit two unterminated bonds per manganese, whereas the {100} surface exhibit one unterminated bond per manganese, which penalizes the {110} surfaces, compared to the {100} surface. Considering the outermost layer of atoms in the rock salt structure, atoms on the {100} surface exhibit one unterminated bond, atoms on the {110} facet exhibit two unterminated bonds, and atoms on the {111} and {112} surface have three

https://doi.org/10.1021/acs.chemmater.2c00804
Chem. Mater. XXXX, XXX, XXX−XXX

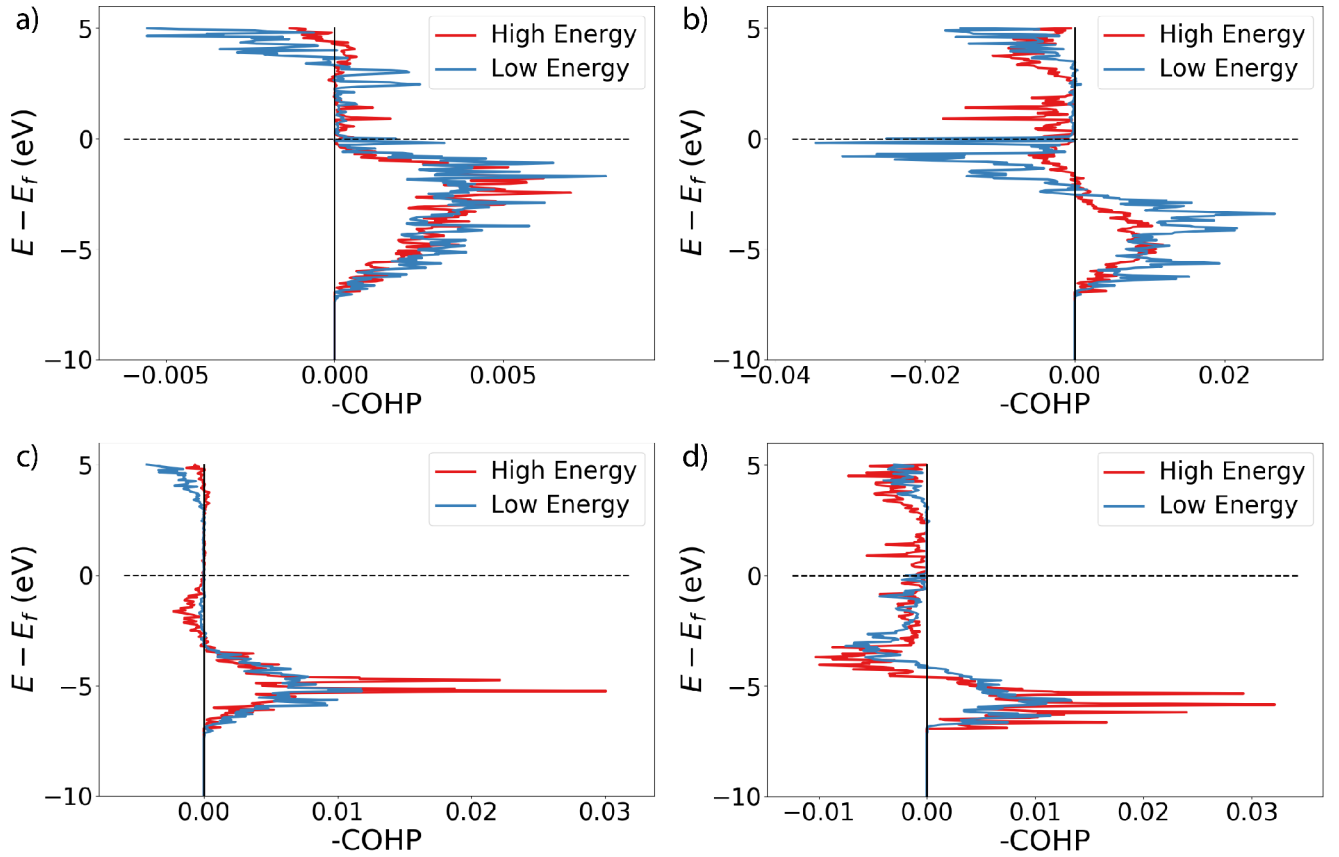

Figure 9. Per-bonding interaction −COHP is plotted for (a) Li 2s−O 2p, (b) Mn 3d−O 2p, (c) Li 2s−F 2p, and (d) Mn 3d−F 2p. Positive values indicate bonding while negative values indicate antibonding.

unterminated bonds. A linear regression of the relationship between the number of unterminated bonds per atom on the outermost layer versus the Boltzmann-weighted surface energy at 298 K predicts that, for each additional unterminated bond per atom on the surface, one would expect an additional 0.24 J/m^2 of surface energy.

Generally, our results indicate that surface enrichment of lithium and fluorine are energetically favorable. The lowest energy surface calculated for each of the four facets are shown in Figure 5. There is no manganese present, expect for a small amount on the {100} and {112} surfaces. The corresponding equilibrium particle shape with the surface chemistry of the lowest calculated {100} surface is shown in Figure 6. Beyond the insights gained for this particular disordered oxide material, we suggest that the chemical stability trends with surface coordination may be used in future studies to advise favorable surface populations and accelerate our characterization of spontaneous surface chemistry formation.

To estimate the range of possible surface energies and equilibrium particle shapes one might obtain by using a sample to approximate the total population of surfaces, a boot-strapping method was again employed to resample the data with replacement. These resampled data were then used to recalculate the Boltzmann-weighted surface energies and resulting equilibrium particle shape. After 10 000 resamplings, it was found that, in 99.75% of the equilibrium particle shapes, the {100} type facet completely dominates to create a cube shape. However, in 0.25% of the resamplings, the {110} and/or {112} type facet appeared in the equilibrium particle shape, creating a slightly chamfered cube shape. Figure 7 shows the cases for which the {110} and {112} facets, among all resamplings, cover their largest fraction of the surface area of the equilibrium particle shape (however, even in these most extreme cases, the {100} type facet still comprises the majority of the surface area of the equilibrium particle shape). The {111} type facet never appeared in the resampling.

In the context of Li-ion energy storage applications, we note that the spontaneous thermodynamic driving force for surface enrichment of lithium and fluorine observed for disordered Li_2MnO_2F is a potential significant advantage for four distinct reasons. First, as lithium migration is faciliated through 0-TM channels[6]—tetrahedral lithium migration sites that face share with no transition-metal cations (hence the name 0-TM)—lithium enrichment bodes well for ion conductivity near the surface of these materials. Second, surface fluorine enrichment or fluorine-containing coatings have been shown to protect against cathode surface deterioration, e.g., acid attack by HF.[51,52] Third, since manganese dissolution is a known source of Li-ion battery degradation and capacity fade,[53−56] a natural surface enrichment of more robust species is likely to correlate with an improvement in capacity retention under otherwise similar conditions. Lastly, oxygen loss[9−11] at high voltage may be partially remedied by fluorine enrichment of the surface, such that oxygen evolution from the surface is kinetically hindered simply by increased diffusion lengths.

In order to further understand the trends in surface energy observed, the density of states of the highest energy and lowest energy surfaces of the {100} type facet was obtained. The choice of facet is motivated by being the most stable, computed facet and experimental observation in DRX

https://doi.org/10.1021/acs.chemmater.2c00804
Chem. Mater. XXXX, XXX, XXX−XXX

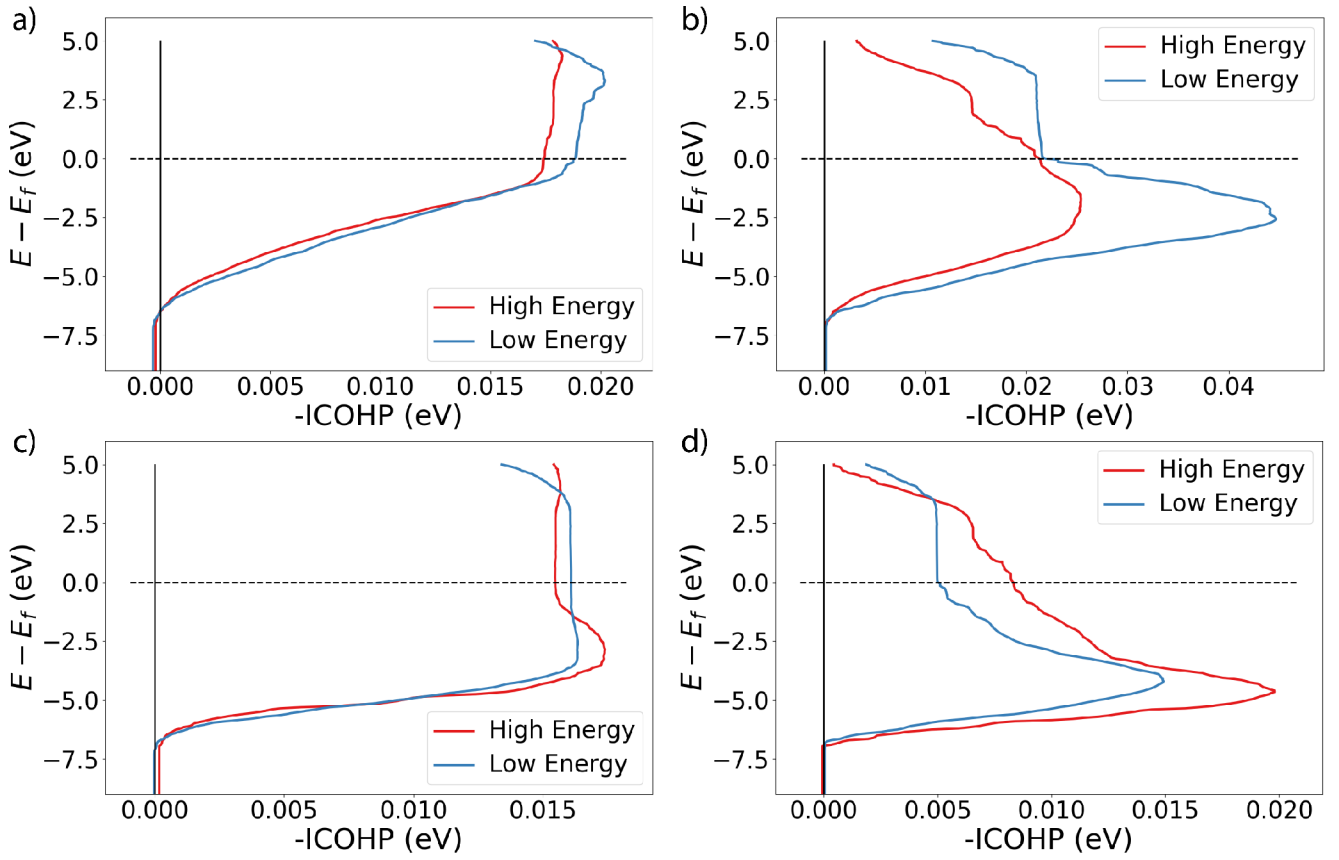

Figure 10. Per-bonding interaction −ICOHP is plotted for (a) Li 2s−O 2p, (b) Mn 3d−O 2p, (c) Li 2s−F 2p, and (d) Mn 3d−F 2p. The value at the Fermi level gives a measure of the bonding or antibonding character overall for these particular types of bonding at the surface.

compounds. Figure 8 shows the partial density of states projected onto the outermost surface layer for the two extreme cases, plotted with the Sumo software.[57] Comparing the high and low energy surfaces, the high energy surface shows a significant spillover of states within the band gap, compared to the low energy surface. In particular, hybridized Mn d-states and O p-states representing undercoordinated atoms are strongly represented. In contrast, the most stable lithium- and fluorine-rich {100} type facet show a distinct absence of gap states. Previous work[58,59] have shown gap states to correlate with defects and/or dangling bonds, which can increase the surface energy,[60] which agrees with our findings here. Specifically, the lithium- and fluorine-rich surfaces are highly ionic in character, with complete charge transfer between the species, which, in turn, minimizes the occurrence of unbound orbitals (as compared to, e.g., manganese) and correlates with low surface energy and enhanced stability. The appearance of oxygen and manganese surface states within the gap (and corresponding lack of lithium or fluorine states) further explains the trends observed that surface oxygen and manganese increase the surface energy while lithium and fluorine generally lower surface energy.

To obtain a more quantitative understanding of the bonding-originated differences in surface energy, we calculate the Crystal Orbital Hamilton Populations (COHP) among atoms in the single, outermost layer of the highest and lowest energy {100} surfaces, using the LOBSTER software.[44−47] The analysis partitions the band structure energy into bonding, nonbonding, and antibonding contributions, which provides an intuitive picture of the chemical bonding of the system. Figure 9 shows the −COHP for four different bonding interactions in Li_2MnO_2F. All bonding interactions of each type were summed for each graph (for example, Li 2s−O 2p contains the sum of all 2s−2p_x, 2s−2p_y, and 2s−2p_z interactions). Because the atomic compositions on the surface are different between the low and high energy surfaces, the values in each graph have been normalized by the number of bonding interactions, and −COHP is plotted per bonding interaction. The general trends in the locations of bonding and antibonding interactions are similar between the high and low energy {100} surfaces, with the exception of the Li 2s−F 2p interaction where there is significant antibonding character just below the Fermi level of the high energy surface that is not observed in the low energy surface. Figure 10 shows the negative integrated Crystal Orbital Hamilton Populations (−ICOHP), which are obtained by integrating over the −COHP plots of Figure 9. More positive values indicate more bonding character, and the value at the Fermi level indicates the per-bond normalized level of bonding character for each type of orbital interaction. For the lower energy surface, all of the calculated bonding interactions exhibited more bonding character than the high energy surface, with the exception of the Mn 3d−F 2p interaction, which is known to be unfavorable.[15,61] The observed result of the lower energy surface having more bonding character for the majority of its bonding interactions than the higher-energy surface provides a quantitative explanation for the difference in surface energies observed. This relationship between the bonding character among surface atoms and the resulting surface energy, may, with further study, be used to design optimal

https://doi.org/10.1021/acs.chemmater.2c00804
Chem. Mater. XXXX, XXX, XXX−XXX

particle morphologies using target synthesis and processing techniques.

CONCLUSIONS

A novel method for creating disordered surfaces that allows for the calculation of surface energies was developed. The method was employed to calculate the surface energies of various bulk as well as surface atomic arrangements of {100}, {110}, {111}, and {112} type surfaces of the disordered rocksalt cathode material Li_2MnO_2F. The {100} type surface was found to exhibit the lowest energy, followed by the {110} facet, both of which have been observed experimentally in DRX compounds. The obtained energies were Boltzmann-weighted to obtain an average energy for each facet, which were then used to obtain the equilibrium cube-like particle shape, with predominant {100} type facets. A statistical analysis and subsequent linear regression indicated that stable surfaces were likely enriched in lithium and fluorine, which, in the context of energy storage applications, correlate with improved cycle life and manganese as well as oxygen retention. The surface electron density of states showed a large amount of gap states in the highest energy {100} surface which was absent in its lowest energy {100} counterpart, providing qualitative evidence for the difference in energy between the two. Consistent with previous bulk work on DRX cathodes, lithium and fluorine interactions were generally found to promote surface stability, while manganese- and oxygen-rich surfaces showed the opposite trend. Surface bonding analysis showed that the majority of interactions in the lowest surface energy {100} surface exhibits more bonding character than the highest energy surface, providing a quantitative explanation for this difference in surface energy.

AUTHOR INFORMATION

Corresponding Authors

Jordan Burns − *Energy Storage and Distributed Resources Division, Lawrence Berkeley National Laboratory, Berkeley, California 94720, United States; Department of Materials Science and Engineering, University of California, Berkeley, California 94720, United States;* orcid.org/0000-0003-0066-2066; Email: jburns@lbl.gov

Kristin A. Persson − *Department of Materials Science and Engineering, University of California, Berkeley, California 94720, United States; Molecular Foundry, Energy Sciences Area, Lawrence Berkeley National Laboratory, Berkeley, California 94720, United States;* orcid.org/0000-0003-2495-5509; Email: kapersson@lbl.gov

Authors

Bin Ouyang − *Department of Materials Science and Engineering, University of California, Berkeley, California 94720, United States; Materials Science Division, Lawrence Berkeley National Laboratory, Berkeley, California 94720, United States;* orcid.org/0000-0002-8181-6815

Jianli Cheng − *Energy Storage and Distributed Resources Division, Lawrence Berkeley National Laboratory, Berkeley, California 94720, United States;* orcid.org/0000-0002-0302-7861

Matthew K. Horton − *Materials Science Division, Lawrence Berkeley National Laboratory, Berkeley, California 94720, United States; Department of Materials Science and Engineering, University of California, Berkeley, California 94720, United States;* orcid.org/0000-0001-7777-8871

Martin Siron − *Materials Science Division, Lawrence Berkeley National Laboratory, Berkeley, California 94720, United States; Department of Materials Science and Engineering, University of California, Berkeley, California 94720, United States;* orcid.org/0000-0002-4562-7814

Oxana Andriuc − *Department of Chemistry, University of California, Berkeley, California 94720, United States; Liquid Sunlight Alliance and Chemical Sciences Division, Lawrence Berkeley National Laboratory, Berkeley, California 94720, United States;* orcid.org/0000-0002-4011-3339

Ruoxi Yang − *Materials Science Division, Lawrence Berkeley National Laboratory, Berkeley, California 94720, United States;* orcid.org/0000-0001-8225-5856

Gerbrand Ceder − *Department of Materials Science and Engineering, University of California, Berkeley, California 94720, United States;* orcid.org/0000-0001-9275-3605

Complete contact information is available at: https://pubs.acs.org/10.1021/acs.chemmater.2c00804

Notes

The authors declare no competing financial interest.

ACKNOWLEDGMENTS

This work was supported by the Assistant Secretary for Energy Efficiency and Renewable Energy, Vehicle Technologies Office, of the U.S. Department of Energy under Contract No. DEAC02-05CH11231 and DE-LC-000L053 under the program of Next Generation Cathode. This research also used resources of the National Energy Research Scientific Computing Center (NERSC), a U.S. Department of Energy Office of Science User Facility located at Lawrence Berkeley National Laboratory, operated under Contract No. DE-AC02-05CH11231. The authors would like to thank Caitlin McCandler and Joey Montoya for stimulating conversations about surfaces.

REFERENCES

(1) Fishman, E.; Cherry, C. E-bikes in the Mainstream: Reviewing a Decade of Research. *Transport Reviews* **2016**, *36*, 72−91.

(2) Kittner, N.; Lill, F.; Kammen, D. M. Energy storage deployment and innovation for the clean energy transition. *Nature Energy* **2017**, *2*, 1−6.

(3) Amnesty International. This is What We Die for: Human Rights Abuses in the Democratic Republic of the Congo Power the Global Trade in Cobalt. *Amnesty Int.* **2016**, AFR 62/3412/2016.

(4) Olivetti, E. A.; Ceder, G.; Gaustad, G. G.; Fu, X. Lithium-Ion Battery Supply Chain Considerations: Analysis of Potential Bottlenecks in Critical Metals. *Joule* **2017**, *1*, 229−243.

(5) Fraser, J.; Anderson, J.; Lazuen, J.; Lu, Y.; Heathman, O.; Brewster, N.; Bedder, J.; Masson, O. *Study on Future Demand and Supply Security of Nickel for Electric Vehicle Batteries*; Publications Office of the European Union, Luxembourg, 2021.

(6) Lee, J.; Urban, A.; Li, X.; Su, D.; Hautier, G.; Ceder, G. Unlocking the potential of cation-disordered oxides for rechargeable lithium batteries. *Science* **2014**, *343*, 519−522.

(7) Clément, R. J.; Lun, Z.; Ceder, G. Cation-disordered rocksalt transition metal oxides and oxyfluorides for high energy lithium-ion cathodes. *Energy Environ. Sci.* **2020**, *13*, 345−373.

(8) Chen, D.; Ahn, J.; Chen, G. An Overview of Cation-Disordered Lithium-Excess Rocksalt Cathodes. *ACS Energy Letters* **2021**, 1358−1376.

(9) Lee, E.; Persson, K. A. Structural and Chemical Evolution of the Layered Li-Excess LixMnO3 as a Function of Li Content from First-Principles Calculations. *Adv. Energy Mater.* **2014**, *4*, 1400498.

(10) Dogan, F.; Croy, J. R.; Balasubramanian, M.; Slater, M. D.; Iddir, H.; Johnson, C. S.; Vaughey, J. T.; Key, B. Solid State NMR Studies of Li 2 MnO 3 and Li-Rich Cathode Materials: Proton Insertion, Local Structure, and Voltage Fade. *J. Electrochem. Soc.* **2015**, *162*, A235−A243.
(11) Shin, Y.; Ding, H.; Persson, K. A. Revealing the Intrinsic Li Mobility in the Li 2 MnO 3 Lithium-Excess Material. *Chem. Mater.* **2016**, *28*, 2081−2088.
(12) Lebens-Higgins, Z.; Chung, H.; Temprano, I.; Zuba, M.; Wu, J.; Rana, J.; Mejia, C.; Jones, M. A.; Wang, L.; Grey, C. P.; Du, Y.; Yang, W.; Meng, Y. S.; Piper, L. F. J. Electrochemical Utilization of Iron IV in the $Li_{1.3}Fe_{0.4}Nb_{0.3}O_2$ Disordered Rocksalt Cathode. *Batteries Supercaps* **2021**, *4*, 771−777.
(13) Chen, D.; Kan, W. H.; Chen, G. Understanding Performance Degradation in Cation-Disordered Rock-Salt Oxide Cathodes. *Adv. Energy Mater.* **2019**, *9*, 1901255.
(14) Yue, Y.; Li, N.; Li, L.; Foley, E. E.; Fu, Y.; Battaglia, V. S.; Clément, R. J.; Wang, C.; Tong, W. Redox Behaviors in a Li-Excess Cation-Disordered Mn-Nb-O-F Rocksalt Cathode. *Chem. Mater.* **2020**, *32*, 4490−4498.
(15) Richards, W. D.; Dacek, S. T.; Kitchaev, D. A.; Ceder, G. Fluorination of Lithium-Excess Transition Metal Oxide Cathode Materials. *Adv. Energy Mater.* **2018**, *8*, 1701533.
(16) House, R. A.; Jin, L.; Maitra, U.; Tsuruta, K.; Somerville, J. W.; Förstermann, D. P.; Massel, F.; Duda, L.; Roberts, M. R.; Bruce, P. G. Lithium manganese oxyfluoride as a new cathode material exhibiting oxygen redox. *Energy Environ. Sci.* **2018**, *11*, 926−932.
(17) Lee, J.; Papp, J. K.; Clément, R. J.; Sallis, S.; Kwon, D.-H.; Shi, T.; Yang, W.; McCloskey, B. D.; Ceder, G. Mitigating oxygen loss to improve the cycling performance of high capacity cation-disordered cathode materials. *Nat. Commun.* **2017**, *8*, 981.
(18) Ahn, J.; Chen, D.; Chen, G. A Fluorination Method for Improving Cation-Disordered Rocksalt Cathode Performance. *Adv. Energy Mater.* **2020**, *10*, 2001671.
(19) Lee, J.; Kitchaev, D. A.; Kwon, D.-H.; Lee, C.-W.; Papp, J. K.; Liu, Y.-S.; Lun, Z.; Clément, R. J.; Shi, T.; McCloskey, B. D.; Guo, J.; Balasubramanian, M.; Ceder, G. Reversible Mn2+/Mn4+ double redox in lithium-excess cathode materials. *Nature* **2018**, *556*, 185−190.
(20) Ouyang, B.; Artrith, N.; Lun, Z.; Jadidi, Z.; Kitchaev, D. A.; Ji, H.; Urban, A.; Ceder, G. Effect of Fluorination on Lithium Transport and Short-Range Order in Disordered-Rocksalt-Type Lithium-Ion Battery Cathodes. *Adv. Energy Mater.* **2020**, *10*, 1903240.
(21) Lun, Z.; Ouyang, B.; Kitchaev, D. A.; Clément, R. J.; Papp, J. K.; Balasubramanian, M.; Tian, Y.; Lei, T.; Shi, T.; McCloskey, B. D.; Lee, J.; Ceder, G. Improved Cycling Performance of Li-Excess Cation-Disordered Cathode Materials upon Fluorine Substitution. *Adv. Energy Mater.* **2019**, *9*, 1802959.
(22) Crafton, M. J.; Yue, Y.; Huang, T. Y.; Tong, W.; McCloskey, B. D. Anion Reactivity in Cation-Disordered Rocksalt Cathode Materials: The Influence of Fluorine Substitution. *Adv. Energy Mater.* **2020**, *10*, 2001500.
(23) Yue, Y.; Li, N.; Ha, Y.; Crafton, M. J.; McCloskey, B. D.; Yang, W.; Tong, W. Tailoring the Redox Reactions for High-Capacity Cycling of Cation-Disordered Rocksalt Cathodes. *Adv. Funct. Mater.* **2021**, *31*, 2008696.
(24) Kwon, D. H.; Lee, J.; Artrith, N.; Kim, H.; Wu, L.; Lun, Z.; Tian, Y.; Zhu, Y.; Ceder, G. The Impact of Surface Structure Transformations on the Performance of Li-Excess Cation-Disordered Rocksalt Cathodes. *Cell Reports Physical Science* **2020**, *1*, 100187.
(25) Linze, L.; Lun, Z.; Chen, D.; Yue, Y.; Tong, W.; Chen, G.; Ceder, G.; Wang, C. Fluorination-Enhanced Surface Stability of Cation-Disordered Rocksalt Cathodes for Li-Ion Batteries. *Adv. Funct. Mater.* **2021**, *31*, 2101888.
(26) Chen, D.; Ahn, J.; Self, E.; Nanda, J.; Chen, G. Understanding cation-disordered rocksalt oxyfluoride cathodes. *J. Mater. Chem. A* **2021**, *9*, 7826−7837.
(27) Shin, Y.; Persson, K. A. Surface Morphology and Surface Stability against Oxygen Loss of the Lithium-Excess Li 2 MnO 3 Cathode Material as a Function of Lithium Concentration. *ACS Appl. Mater. Interfaces* **2016**, *8*, 25595−25602.
(28) Karim, A.; Fosse, S.; Persson, K. A. Surface structure and equilibrium particle shape of the LiMn 2O4 spinel from first-principles calculations. *Phys. Rev. B* **2013**, *87*, 25−28.
(29) Warburton, R. E.; Iddir, H.; Curtiss, L. A.; Greeley, J. Thermodynamic Stability of Low- and High-Index Spinel LiMn2O4 Surface Terminations. *ACS Appl. Mater. Interfaces* **2016**, *8*, 11108−11121.
(30) Ringe, E.; Van Duyne, R. P.; Marks, L. D. Wulff construction for alloy nanoparticles. *Nano Lett.* **2011**, *11*, 3399−3403.
(31) Fontaine, D. D. *Solid State Physics—Advances in Research and Applications*; Academic Press, 1994; pp 33−176.
(32) Sanchez, J.M.; Ducastelle, F.; Gratias, D. Generalized cluster description systems. *Physica A* **1984**, *128*, 334−350.
(33) Metropolis, N.; Rosenbluth, A. W.; Rosenbluth, M. N.; Teller, A. H.; Teller, E. Equation of state calculations by fast computing machines. *J. Chem. Phys.* **1953**, *21*, 1087−1092.
(34) Hastings, W. K. Monte Carlo sampling methods using Markov chains and their applications. *Biometrika* **1970**, *57*, 97−109.
(35) Tepesch, P. D.; Garbulsky, G. D.; Ceder, G. Model for configurational thermodynamics in ionic systems. *Phys. Rev. Lett.* **1995**, *74*, 2272−2275.
(36) Kresse, G.; Hafner, J. Ab initio molecular dynamics for liquid metals. *Phys. Rev. B* **1993**, *47*, 558−561.
(37) Kresse, G.; Hafner, J. Ab initio molecular-dynamics simulation of the liquid-metalamorphous- semiconductor transition in germanium. *Phys. Rev. B* **1994**, *49*, 14251−14269.
(38) Kresse, G.; Furthmüller, J. Efficiency of ab-initio total energy calculations for metals and semiconductors using a plane-wave basis set. *Comput. Mater. Sci.* **1996**, *6*, 15−50.
(39) Kresse, G.; Furthmüller, J. Efficient iterative schemes for ab initio total-energy calculations using a plane-wave basis set. *Phys. Rev. B* **1996**, *54*, 11169−11186.
(40) Blöchl, P. E. Projector augmented-wave method. *Phys. Rev. B* **1994**, *50*, 17953−17979.
(41) Perdew, J. P.; Burke, K.; Ernzerhof, M. Generalized gradient approximation made simple. *Phys. Rev. Lett.* **1996**, *77*, 3865−3868.
(42) Ong, S. P.; Richards, W. D.; Jain, A.; Hautier, G.; Kocher, M.; Cholia, S.; Gunter, D.; Chevrier, V. L.; Persson, K. A.; Ceder, G. Python Materials Genomics (pymatgen): A robust, open-source python library for materials analysis. *Comput. Mater. Sci.* **2013**, *68*, 314−319.
(43) Barber, C. B.; Dobkin, D. P.; Huhdanpaa, H. The Quickhull Algorithm for Convex Hulls. *ACM Trans. Math. Software* **1996**, *22*, 469−483.
(44) Maintz, S.; Deringer, V. L.; Tchougréeff, A. L.; Dronskowski, R. Analytic projection from plane-wave and PAW wavefunctions and application to chemical-bonding analysis in solids. *J. Comput. Chem.* **2013**, *34*, 2557−2567.
(45) Deringer, V. L.; Tchougréeff, A. L.; Dronskowski, R. Crystal orbital Hamilton population (COHP) analysis as projected from plane-wave basis sets. *J. Phys. Chem. A* **2011**, *115*, 5461−5466.
(46) Dronskowski, R.; Blochl, P. E. Crystal Orbital Hamiltonian Populations (COHP). Energy-Resolved Visualization of Chemical Bonding in Solids Based on Density-Functional Calculations. *J. Phys. Chem.* **1993**, *97*, 8617−8624.
(47) Maintz, S.; Deringer, V. L.; Tchougréeff, A. L.; Dronskowski, R. LOBSTER: A tool to extract chemical bonding from plane-wave based DFT. *J. Comput. Chem.* **2016**, *37*, 1030−1035.
(48) Tran, R.; Xu, Z.; Radhakrishnan, B.; Winston, D.; Sun, W.; Persson, K. A.; Ong, S. P. Surface energies of elemental crystals. *Sci. Data* **2016**, *3*, 160080.
(49) Chen, D.; Zhang, J.; Jiang, Z.; Wei, C.; Burns, J.; Li, L.; Wang, C.; Persson, K.; Liu, Y.; Chen, G. Role of Fluorine in Chemo-mechanics of Cation-Disordered Rocksalt Cathodes. *Chem. Mater.* **2021**, *33*, 7028−7038.
(50) Waskom, M. Seaborn: Statistical Data Visualization. *J. Open Source Software* **2021**, *6*, 3021.

https://doi.org/10.1021/acs.chemmater.2c00804
Chem. Mater. XXXX, XXX, XXX−XXX

(51) Yue, P.; Wang, Z.; Guo, H.; Xiong, X.; Li, X. A low temperature fluorine substitution on the electrochemical performance of layered LiNi0.8Co0.1Mn0.1O 2-zFz cathode materials. *Electrochim. Acta* **2013**, *92*, 1−8.
(52) Lee, S. H.; Yoon, C. S.; Amine, K.; Sun, Y. K. Improvement of long-term cycling performance of Li[Ni0.8Co 0.15Al0.05]O2 by AlF3 coating. *J. Power Sources* **2013**, *234*, 201−207.
(53) Zhan, C.; Lu, J.; Jeremy Kropf, A.; Wu, T.; Jansen, A. N.; Sun, Y. K.; Qiu, X.; Amine, K. Mn(II) deposition on anodes and its effects on capacity fade in spinel lithium manganate-carbon systems. *Nat. Commun.* **2013**, *4*, 1−8.
(54) Kim, J. S.; Kim, K.; Cho, W.; Shin, W. H.; Kanno, R.; Choi, J. W. A truncated manganese spinel cathode for excellent power and lifetime in lithium-ion batteries. *Nano Lett.* **2012**, *12*, 6358−6365.
(55) Liu, T.; et al. Correlation between manganese dissolution and dynamic phase stability in spinel-based lithium-ion battery. *Nat. Commun.* **2019**, *10*, 4721.
(56) Tang, D.; Sun, Y.; Yang, Z.; Ben, L.; Gu, L.; Huang, X. Surface structure evolution of LiMn2O4 cathode material upon charge/discharge. *Chem. Mater.* **2014**, *26*, 3535−3543.
(57) M Ganose, A.; J Jackson, A.; O Scanlon, D. sumo: Command-line tools for plotting and analysis of periodic ab initio calculations. *Journal of Open Source Software* **2018**, *3*, 717.
(58) Herbert, F. W.; Krishnamoorthy, A.; Van Vliet, K. J.; Yildiz, B. Quantification of electronic band gap and surface states on FeS 2(100). *Surf. Sci.* **2013**, *618*, 53−61.
(59) Lin, L.; Robertson, J. Defect states at III-V semiconductor oxide interfaces. *Appl. Phys. Lett.* **2011**, *98*, 082903.
(60) Rimsza, J. M.; Foiles, S.; Michael, J.; Mackie, W.; Larson, K. Role of defects on the surface properties of HfC. *Appl. Surf. Sci.* **2019**, *495*, 143500.
(61) Clement, R. J.; Kitchaev, D.; Lee, J.; Gerbrand Ceder. Short-Range Order and Unusual Modes of Nickel Redox in a Fluorine-Substituted Disordered Rocksalt Oxide Lithium-Ion Cathode. *Chem. Mater.* **2018**, *30*, 6945−6956.

https://doi.org/10.1021/acs.chemmater.2c00804
Chem. Mater. XXXX, XXX, XXX−XXX